Research Square

Preprints are preliminary reports that have not undergone peer review.
They should not be considered conclusive, used to inform clinical practice,
or referenced by the media as validated information.

Metabolic profiling of retinal organoids reveals conserved core metabolites and alterations in glycolytic, and amino acid pathways

Pragati Gupta
Radboud University Medical Centre
Claudia Wiesner
Leipzig University
Focke Zimmsen
Leipzig University
Jeroen Klevering
Radboud University Medical Centre
Purva Kulkarini
Radboud University Medical Centre
Zohreh Hosseinzadeh
Zohreh.hosseinzadeh@radboudumc.nl
Radboud University Medical Centre

Research Article

Keywords: retinal organoids, mouse retina, metabolomics, GCMS (Gas chromatography-mass spectrometry)

Posted Date: July 7th, 2026

DOI: https://doi.org/10.21203/rs.3.rs-10181802/v1

License: This work is licensed under a Creative Commons Attribution 4.0 International License.
Read Full License

Additional Declarations: No competing interests reported.

Version of Record: A version of this preprint was published at Metabolomics on October 10th, 2026. See the published version at https://doi.org/10.1007/s11306-026-02523-4.

Abstract

Introduction:

Retinal organoids have emerged as powerful models of retinal development and disease; however, the extent to which they recapitulate the metabolic landscape of the native retina remains largely unknown.

Objectives

This study aimed to compare the metabolomic profiles of mouse retina and mouse embryonic stem cell-derived retinal organoids and to evaluate metabolic changes during organoid maturation.

Methods

Untargeted gas chromatography mass spectrometry (GCMS) based metabolomic profiling was performed on intracellular metabolites from mouse retina and mouse retinal organoids (MRO), together with media collected during organoid maturation. Statistical, visualization and pathway enrichment analyses were performed.

Results

A total of 166 metabolites were detected in both mouse retina and MRO. 29 were significantly altered, while 15 metabolites were detected only in mouse retina and 3 in retinal organoids. Retinal organoids have emerged as powerful models of retinal development and disease; however, the extent to which they recapitulate the metabolic landscape of the native retina remains largely unknown. preserved a substantial conserved retinal metabolic signature but demonstrated selective divergence in glycolysis-associated metabolites and pentose phosphate pathway intermediates including glucose-6-phosphate and ribulose-5-phosphate, as well as tricarboxylic acid-cycle-associated (TCA) metabolites including citric acid, fumaric acid and oxalic acid. Pathway analysis identified significant alterations in alanine, aspartate, and glutamate metabolism. Media analysis further revealed stage-dependent increases in extracellular glutamate and glycine abundance during organoid maturation.

Conclusion

MRO retain major components of retinal metabolic organization while exhibiting features suggestive of incomplete metabolic maturation compared with native retina. These findings provide valuable insight into MRO metabolic fidelity and guide future optimization strategies.

1. Introduction

The retina is among the most metabolically active tissues in the body, requiring tightly coordinated energy production, redox homeostasis, and biosynthetic capacity to sustain phototransduction, synaptic transmission, and continuous outer segment renewal (Du *et al.*, 2016; Hurley *et al.*, 2015). Photoreceptors rely heavily on aerobic glycolysis, mitochondrial oxidative phosphorylation, and lipid metabolism to meet these demands, while Müller glia and the retinal pigment epithelium provide critical metabolic support through lactate shuttling, antioxidant buffering, and nutrient recycling (Li *et al.*, 2020; Viegas and Neuhauss, 2021).

Direct functional measurements in isolated mouse retina demonstrate that retinal energy metabolism is dynamically regulated by neuronal activity, with flicker stimulation inducing rapid increases in oxygen consumption and metabolic flux, highlighting the tight coupling between retinal function and metabolic demand (Linsenmeier and Dmitriev, 2024). Real-time bioenergetic profiling of dissociated mouse photoreceptors further shows that these cells maintain distinct glycolytic and mitochondrial respiration programs (Yera *et al.*, 2025). Recent studies have highlighted metabolism as a critical determinant of retinal development and function. In the mouse retina, photoreceptors preferentially convert glucose to lactate even under oxygen-rich conditions, while channeling mitochondrial metabolism toward biosynthesis rather than maximal ATP production (Li *et al.*, 2020). Age-dependent remodeling of glycolysis, the tricarboxylic acid (TCA) cycle, amino acid metabolism, and redox pathways has been documented in mouse retina and retinal pigment epithelium (Tsantilas *et al.*, 2021). Large-scale metabolomic profiling of mouse fetal organs reveals that metabolic pathway composition is organ-specific and developmentally regulated, indicating that metabolic identity is a defining feature of tissue maturation rather than a secondary consequence of differentiation (Li *et al.*, 2025). Consistent with this, early mouse embryogenesis is characterized by extensive metabolic remodeling across glycolysis, the TCA cycle, and lipid metabolism, and disruption of these processes impairs developmental progression, demonstrating a causal role for metabolic programming in tissue maturation (Zhao *et al.*, 2021). Importantly, metabolic specialization differs not only across developmental time but also between rods and cones, retinal regions, and supporting cell types, suggesting that incomplete metabolic patterning may directly limit organoid functionality.

Pluripotent stem cell–derived retinal organoids have emerged as a powerful complementary model system to *in vivo* mouse studies, offering several experimental advantages for studying retinal development and disease mechanisms (Cowan *et al.*, 2020; Eiraku *et al.*, 2011; Kim *et al.*, 2019). Unlike in vivo mouse models, mouse retinal organoids (MRO) can be generated in large numbers from a single differentiation batch, enabling parallel experimentation, improved reproducibility, and systematic manipulation of culture conditions that are difficult to achieve in vivo (Kim *et al.*, 2019; La Torre, 2016). This scalability facilitates high-throughput molecular profiling and controlled perturbation studies, while reducing animal usage and experimental variability (Hanna *et al.*, 2022).

At the RNA level, bulk transcriptomics data show that retinal organoids recapitulate key gene expression programs of retinal development, photoreceptor differentiation, and synaptic signalling, but exhibit partial metabolic divergence from native retina (Cui *et al.*, 2020). Most major retinal cell classes are

present in organoids, their molecular identities often correspond to earlier developmental stages compared with native retina, particularly for photoreceptors and metabolically demanding neuronal subtypes (Cowan *et al.*, 2020; Sridhar *et al.*, 2020). The genes associated with energy metabolism, mitochondrial function, lipid biosynthesis, and neurotransmitter cycling are expressed in retinal organoids, indicating partial activation of retinal metabolic pathways at the RNA level (Cui *et al.*, 2020). In the retinal organoids, deficiencies in lipid uptake, fatty acid elongation, and β-oxidation have been linked to impaired outer segment development and photoreceptor vulnerability, further emphasizing the need to address metabolic insufficiencies to achieve functional parity with native retina (West *et al.*, 2022). However, transcriptomic and proteomic profiling alone cannot capture actual metabolite abundance or pathway flux, and therefore do not directly reflect the functional metabolic state of retinal organoids (Cui *et al.*, 2020). Given that the retina is among the most metabolically demanding tissues in the body, relying heavily on tightly regulated glucose, lipid, and amino acid metabolism to sustain phototransduction and synaptic transmission (Hanna *et al.*, 2022; Viegas and Neuhauss, 2021), indirect molecular readouts may overlook critical metabolic deficiencies affecting organoid maturation. Several studies have developed MRO (Chen *et al.*, 2020; La Torre, 2016; Völkner *et al.*, 2021). Compared with human retinal organoids (> 200days), they exhibit a shorter maturation time (> 28days) and are more cost-effective. In addition, they can be generated at a large scale in a single batch compared with mouse retina preparation (Chen *et al.*, 2020; La Torre, 2016; Völkner *et al.*, 2021) Therefore, this study uses MRO as an efficient model to support the 3R principles (reduction, replacement, refinement) and to investigate their metabolic profile at maturity.

In this study, we systematically compare the metabolic landscape of stem cell-derived MRO with that of native mouse retina using untargeted metabolomic profiling and pathway enrichment analysis. By mapping significant differential metabolites to canonical metabolic pathways, we aim to pinpoint actionable targets for culture optimization and experimental modulation in the future.

2. Materials and Methods

2.1 Materials and Chemicals

Mouse embryonic stem cells (mESCs; ESD3 line) were cultured using Dulbecco's Modified Eagle Medium (DMEM), high glucose (Gibco™, Cat# 10564-011), Leukemia Inhibitory Factor (LIF; Merck Millipore, Cat# ESG1107), Glasgow's MEM (GMEM; Gibco™, Cat# 11710-035), and DMEM/F12 Ham (Gibco™, Cat# 10565-018) from Thermo Fisher Scientific (Waltham, MA, USA). Media were supplemented with ESC-qualified fetal bovine serum (FBS; Cat# 10439-024), Knock-Out Serum Replacement (KSR; Cat# 10828-028), 10 mM non-essential amino acids (NEAA; Cat# 11140-050), sodium pyruvate (Cat# 11360-070), penicillin-streptomycin (Pen/Strep; Cat# 15140-122), and cell culture-grade water (Cat# 15230-162). TrypLE™ Express (Cat# 12605-028) was used for cell dissociation. Retinal differentiation (RD) was induced with CHIR99021 (GSK3β inhibitor; Stemgent, Cat# 04-0004-02), and PD0325901 (MEK/ERK inhibitor; Stemgent, Cat# 04-0006-02). For optic vesicle and photoreceptor development, we used TOM's medium supplemented with N2 (Gibco™, Cat# 17502-048), B27 (Gibco™, Cat# 17504044), all-trans

retinoic acid (Sigma-Aldrich, Cat# R2625-50MG), taurine (Sigma-Aldrich, Cat# T-8691), and GFR Matrigel® (Corning®, Cat# 356230) (Supplementary table S1). Cultureware included 96-well ultra-low-adhesion Lipidure-Coat plates (AMSbio, Cat# AMS.51011610), 6-well ultra-low-adhesion plates (Corning™, Cat# 07-200-601), and sterile glass Pasteur pipettes. For metabolite extraction and derivatization, methanol, chloroform, and pyridine (all ≥ 99%, Sigma-Aldrich), methoxyamine hydrochloride (Thermo Fisher), and BSTFA (Sigma-Aldrich, ≥ 98.5%) were used.

2.2 Study Design and workflow

Neonatal C57BL/6 retinas (postnatal days 1–7) and day 28 MRO differentiated from ESD3 mouse embryonic stem cells (ESCs) were processed in parallel and analyzed by gas chromatography electron ionization quadrupole mass spectrometry (GC–EI–Q–MS).

We performed an untargeted, comparative metabolomic analysis to assess how closely stem cell derived MRO recapitulate the endogenous metabolome of mouse retina in three steps (Fig. 1).

2.3 Sample Preparation

2.3.1 Animals

All animal experiments were conducted according to the German law for the welfare of animals and approved by the authorities of the state of Saxony. Experiments were performed with retina at postnatal day P1–P7 female and male C57BL/6 mice (Jackson Lab). Eyes from mice were enucleated and simultaneously retinas were dissected under a sterile stereomicroscope and cultured in DMEM (Gibco™, Cat# 10564-011).

2.3.2 MRO differentiation

Mouse ESD3 embryonic stem cells (ESCs) were seeded at a density of 3,000 cells per well in ultra-low-adhesion U-bottom 96-well plates using RD medium. On day-01, 2% (v/v) Matrigel was added to each well to provide laminin- and collagen-rich basement membrane signals essential for optic vesicle morphogenesis and the establishment of epithelial polarity. During the induction phase (days 0–7), organoids were maintained in RD medium to promote early neuroectodermal differentiation and optic vesicle-like structure formation. From days 07–15 (patterning phase), organoids were transferred to 6-well suspension culture plates and maintained in TOM's medium supplemented with N2 and B27, supporting retinal progenitor survival and photoreceptor lineage commitment. Between days 10 to 15, the medium was additionally supplemented with 0.5 µM retinoic acid and 1 mM taurine to enhance photoreceptor specification and protect against oxidative stress. From days 15–28 (maturation phase), organoids were cultured in plain TOM's medium without any supplements to promote terminal differentiation and laminar organization of retinal tissue (Supplementary Table S1).

2.4 Quantitative Real-Time PCR (qPCR) Analysis

2.4.1 RNA Isolation and cDNA Synthesis

Total RNA was isolated from MRO using the NucleoSpin RNA Mini Kit (Macherey-Nagel, #740955.250) according to the manufacturer's protocol with minor modifications. Briefly, five MRO were collected in 1.5 mL microcentrifuge tubes, washed once with 1× phosphate-buffered saline (PBS), and residual buffer was aspirated. Samples not processed immediately were snap-frozen and stored at − 80°C until further use. For RNA extraction, organoids were lysed in RA1 buffer and mechanically homogenized by pipetting (10 repetitions). On-column rDNase digestion was performed to eliminate genomic DNA contamination. RNA was eluted in 30 µL RNase-free water to account for low input material. RNA concentration and purity (A260/280 and A260/230 ratios) were assessed using a NanoDrop spectrophotometer (DeNovix), with RNase-free water as blank. Complementary DNA (cDNA) was synthesized using the iScript™ cDNA Synthesis Kit (Bio-Rad, #170–8891). RNA was diluted in nuclease-free water to a final volume of 15 µL. Reverse transcription reactions were prepared according to the manufacturer's instructions to a final volume of 20 µL. The reaction conditions were as follows: priming at 65°C for 5 minutes, reverse transcription at 46°C for 20 minutes, and enzyme inactivation at 95°C for 1 minute. The resulting cDNA was diluted 1:6 nuclease-free water and stored at − 20°C until further use.

2.4.2 Analysis

Quantitative real-time PCR (qPCR) was performed using GoTaq® qPCR Master Mix (2×; Promega, #A600A). The reaction mixture consisted of PCR-grade water, 10 µM forward and reverse primers, and 1× master mix. Technical triplicates were performed. Gene expression analysis was conducted for the following targets: *Pax6, Prkca*,, and *Opn1sw*. Primer sequences are provided in Supplementary Table S2. For each reaction, 5 µL of cDNA template was combined with 7.5 µL of qPCR master mix in a 384-well plate, which was subsequently sealed with adhesive PCR film. Amplification was performed using the QuantStudio™ 5 Real-Time PCR System (Applied Biosystems, Thermo Fisher Scientific) under standard cycling conditions (Supplementary Table S3). Quantification cycle (Ct) values were obtained using QuantStudio Design & Analysis Software v1.4.3. Relative gene expression was calculated using the comparative ΔΔCt method, with *ACTB* serving as the endogenous reference gene. Expression levels were normalized to undifferentiated mouse embryonic stem cells (mESCs).

2.5 Metabolite extraction and derivatization

2.5.1 Extraction

We developed a pipeline for extraction of metabolites based on a previously established protocol (Du et al., 2016). MRO and mouse retina samples were processed in 3 independent batches for each sample type. The samples were homogenized in 140 µL ice-cold methanol:chloroform:water (70:20:5, *v/v*) buffer by gentle pipetting for 2–5 minutes, vortexed to enhance metabolite solubilization. After incubation on ice for 15 minutes, the samples were centrifuged at 14,000 × g for 15 minutes at 4°C. The supernatant was collected and lyophilised.

2.5.2 Derivatization

Dried extracts were first methoximated by adding 25 µL of 20 mg/mL methoxyamine hydrochloride in pyridine and incubated at 37°C for 90 minutes. Subsequently, 46 µL of *N,O*-bis(trimethylsilyl)trifluoroacetamide (BSTFA) was added for silylation at 70°C for 30 minutes. The derivatized samples were transferred into 1.5 mL GC vials fitted with 0.2 mL glass microinserts and sealed.

2.6 GC–EI–Q–MS Analysis

Samples were analyzed using an Agilent 6890/5973N Plus GCMS system, coupled with electron impact (EI) ionization and a quadrupole mass spectrometer (HP-MSD). This setup enabled high-sensitivity detection and identification of volatile and semi-volatile metabolites. Metabolite separation was achieved on a DB-5MS Ultra Inert column (30 m × 0.25 mm ID, 0.25 µm film; Agilent Technologies, Germany) using helium as the carrier gas at 1.2 mL/min. Injection was performed in splitless mode at 250°C. The oven program started at 60°C (2 min hold), ramped to 320°C at 10°C/min, and held for 5 min. Electron impact ionization was performed at 70 eV with the ion source set to 230°C. Mass spectra were acquired over *m/z* 35–600.

2.7 Data Processing

Raw chromatograms were processed using AMDIS 2.71 for deconvolution. Peaks were annotated by mass spectral comparison with the NIST14 library (National Institute of Standards and Technology, Massachusetts, USA), with retention indices computed using chromatogram-intrinsic retention time standards. Only metabolites with high-confidence spectral matches (similarity score ≥ 800) were retained. Quantitative integration of manually selected ion fragments (*m/z* ± 0.5) was performed using Mass Hunter Quantitative Analysis B.07.00 (Supplementary Excel 1).

2.8 Statistical Analysis

Peak area data obtained from GCMS analysis were imported into the MetaboAnalyst 6.0 (www.metaboanalyst.ca/) platform for statistical evaluation. Data preprocessing included median normalization, missing value imputation using the minimum detected value, log10 transformation, and auto-scaling. Metabolites with FDR < 0.05 and fold change (FC) ≥ 10 were considered significantly altered. Fold change analysis is provided in Supplementary Excel Sheet 2. Differential metabolite abundance between mouse retina and MRO was assessed using unpaired Student's t-test with Benjamini–Hochberg FDR correction (Supplementary Excel Sheet 3), one-way ANOVA for metabolomics of organoid maturation media results in Supplementary Excel Sheet 4. QPCR statistical analyses were performed with the GraphPad Prism 10.4.1 program. Heatmaps of significant metabolites were generated using Euclidean distance and Ward's hierarchical clustering of averaged replicates without autoscaling.

2.9 Pathway Analysis

Metabolites with confirmed annotations were assigned KEGG (Kyoto Encyclopedia of Genes and Genomes) compound identifiers and submitted to MetaboAnalyst 6.0 (www.metaboanalyst.ca) for

pathway topology analysis.

3. Results

3.1 Metabolic profile and characterization of MRO

MRO was generated from mouse embryonic stem cells (mESCs) using a stepwise differentiation protocol recapitulating major stages of retinal development, including embryoid body formation, optic vesicle emergence, optic cup morphogenesis, and retinal maturation (Fig. 2a). Day 28 MRO and postnatal mouse retina (P1–P7) were subjected to GCMS based metabolomic profiling following metabolite extraction and derivatization (Fig. 2b). The selection of day-28 MROs and P1–P7 mouse retina was guided by previous transcriptomic studies showing that MROs at this stage most closely resemble early postnatal retinal development rather than mature adult retina (Cui et al., 2020). Three independent biological replicates derived from independent differentiation batches were analyzed (n = 3). Total ion chromatograms demonstrated broadly similar metabolic profiles between MRO and mouse retina, with aligned retention times across major peaks, indicating preservation of core retinal metabolic features (Fig. 2c). However, reduced peak intensities were observed in MRO for multiple metabolites. Supportive qPCR characterization confirmed retinal lineage specification in day 28 organoids (Fig. 2d). PAX6(retinal niche cell marker), OPN1SW (cone photoreceptor marker), and Prkca (bipolar cell marker) expression levels were significantly increased compared with undifferentiated mESCs.

3.2 Classification metabolites in mouse retina and retinal organoids

Detected metabolites from mouse retina and MRO were classified into major biochemical categories (Fig. 3a). A total of 148 metabolites were common to both systems, whereas 15 metabolites were detected only in mouse retina and 3 metabolite only in MRO (Fig. 3b). Detected metabolites were grouped into amino acids and related derivatives, lipids and fatty acid derivatives, carbohydrates and sugar alcohols, and organic acids (Fig. 3c–f). Amino acid-related metabolites represented the largest metabolite class in both systems, followed by carbohydrates/sugar alcohols and lipid-associated metabolites. Organic acids, including glycolysis- and TCA-cycle-associated metabolites, were also detected in both mouse retina and MRO. Overall, the metabolite class distribution demonstrated broad metabolic overlap between MRO and native mouse retina.

3.3 Unsupervised and supervised clustering of metabolites in MRO

Unsupervised multivariate analyses were performed to compare the metabolic profiles of mouse retina, MRO, and their corresponding culture media using GCMS datasets. Principal component analysis (PCA)

demonstrated clear separation between tissue and media samples, with PC1 accounting for 44.7% of the total variance and PC2 explaining 15.3% (Fig. 3a).

Mouse retina and MRO formed distinct clusters, while the corresponding media samples clustered separately. Hierarchical clustering analysis further confirmed group-specific segregation and showed close clustering of biological replicates, indicating good reproducibility (Fig. 4b). Partial least squares–discriminant analysis (PLS-DA), a supervised multivariate analysis, further demonstrated distinct metabolic separation between mouse retina and MRO (Fig. 4c). Tight clustering of replicates within each group supported within-group consistency. Variable importance in projection (VIP) analysis identified several metabolites contributing strongly to group discrimination (VIP > 1), including pantothenic acid, erythritol, phosphate, glycerol-3-phosphate, and carbohydrate-associated metabolites (Fig. 4d). The PLS-DA PCA biplot of metabolomic profiles from MRO and mouse retina indicated the most strongly to metabolomic group separation. Metabolites with vectors directed toward mouse retina cluster were urea, erythritol, phosphoethanolamine, and pyroglutamic acid), whereas metabolites directed toward the MRO cluster were fructofuranose, galactopyranose, and 1-O-methyl-galactopyranoside (Fig. 4e). Pattern correlation analysis identified coordinated metabolite relationships between mouse retina and MRO (Fig. 4f). Among 148 detected metabolites, 28 metabolites showed highly significant correlations at a stringent threshold of FDR < 0.005, including 19 positively correlated and 9 negatively correlated metabolites.

3.4 Differential metabolite abundance patterns of MRO

Heatmap analysis demonstrated distinct metabolic clustering between mouse retina and MRO across amino acids, organic acids, hydrocarbons, carbohydrates, lipids, and phosphate-associated metabolites (Fig. 5a–f, Fig. S3 and Supplementary Excel Sheet 3 provided analyse). Amino acid and neurotransmitter-associated metabolites, including glutamine, taurine, hypotaurine, and glutamate-related metabolites, generally showed higher abundance in mouse retina, whereas selected amino acid derivatives were relatively enriched in MRO. Organic acid profiling revealed differential abundance of glycolysis and TCA-cycle-associated metabolites, with several glycolytic intermediates reduced in MRO. Carbohydrate profiling demonstrated elevated abundance of several monosaccharides and modified sugars in organoids, while phosphorylated carbohydrate intermediates, including glucose-6-phosphate and related phosphate-containing metabolites, showed lower abundance compared to mouse retina. Lipid and sterol profiling also revealed distinct group-specific abundance patterns between retina and MRO.

Pathway analysis identified significant alterations in arginine biosynthesis, starch, sucrose metabolism, glycine, serine, threonine metabolism, and taurine/hypotaurine metabolism (Fig. 5g). We proposed a metabolic pathway model for MRO based on the metabolomic alterations identified in this study. Compared with native mouse retina, MROs exhibited reduced levels of metabolites involved in glycolysis, the pentose phosphate pathway, TCA, and glutamine/GABA metabolism (Fig. 5h).

3.7 Clustering secretome metabolomics during MRO development

GCMS metabolomic profiling of conditioned media collected during retinal organoid maturation (day 8 to day 28) revealed progressive temporal changes in extracellular metabolite composition (Fig. 5, Fig S5 and Supplementary Excel Sheet 4 provided analyse). Multivariate analysis demonstrated clear stage-dependent clustering of media samples, with early (day 8–10), intermediate (day 13–15), and late (day-28) stages forming distinct groups (Fig. 6a). PLS-DA VIP analysis identified several metabolites contributing strongly to developmental stage separation (Fig. 6b). Hierarchical clustering heatmaps revealed stage-specific remodeling across amino acid, organic acid, carbohydrate, lipid, hydrocarbon, and phosphate-associated metabolites during organoid maturation (Fig. 6c–h). Heatmap visualization further demonstrated temporal changes in metabolite abundance, with several amino acid–related metabolites showing increased abundance at later developmental stages. Organic acid profiles demonstrated pronounced temporal clustering, while metabolites associated with central carbon and carbohydrate metabolism displayed increased abundance during later stages. Lipid and hydrocarbon metabolites exhibited comparatively moderate variation across developmental stages. Glycerol and phosphate-associated metabolites showed distinct fluctuations and clustering patterns across maturation time points.

4. Discussion

In this study aimed to characterize the biochemical profile of MRO to evaluate their potential as an alternative to mouse retina. We discover that MRO preserve a substantial retinal metabolic signature despite selective metabolic divergence. A broad overlap was observed across amino acids, neurotransmitter-associated metabolites, glycolytic intermediates, TCA-cycle metabolites, lipids, sterols, and nucleotide-associated compounds, indicating that MRO recapitulate major components of retinal biochemical organization. Organoid generation is faster and more efficient in terms of material consumption, and it supports the 3R principle (Replacement, Reduction, and Refinement) by minimizing the use of living animals in research.

Conserved retinal metabolic core and selective metabolic divergence

A major finding of this study is that MRO preserve a substantial proportion of the native retinal metabolome. Conserved metabolites included neurotransmitter-associated compounds (glutamate, GABA, taurine), amino acids (glutamine, glycine, alanine, serine, methionine, valine, leucine, and phenylalanine), and TCA-cycle intermediates (citrate, succinate, fumarate, and malate), indicating retention of core retinal neuronal and energy-associated metabolism. Taurine, one of the most abundant metabolites in the vertebrate retina, is essential for retinal development and photoreceptor maintenance (Ripps and Shen, 2012), whereas glutamate and GABA are central mediators of retinal neurotransmission (Du *et al.*, 2016). Together, these findings suggest that MRO maintain a retina-like biochemical identity rather than representing metabolically unrelated in vitro tissue systems.

Despite this broad conservation, several metabolites associated with glycolysis, pentose phosphate metabolism, phospholipid metabolism, and phosphate-associated pathways were not detected in MRO, including glucose-6-phosphate, glycerol-3-phosphate, dihydroxyacetone phosphate, ribulose-5-phosphate, phosphoryl ethanolamine, and myo-inositol. These observations suggest divergence in central carbon metabolism and membrane-associated metabolic pathways. However, because GC–MS detection is influenced by metabolite abundance, extraction efficiency, and derivatization bias, metabolites not detected in organoids should not be interpreted as completely absent (Fiehn et al, 2016).

Central carbon, neurotransmitter, and lipid metabolism

GC-MS metabolomic profiling revealed that mouse retinal organoids preserve a substantial proportion of the metabolic landscape of the native retina while exhibiting selective differences in metabolites associated with energy metabolism, phospholipid metabolism, and neurotransmitter biosynthesis. Multivariate analyses demonstrated clear separation between organoids and retina; however, most detected metabolites were shared between the two tissues, indicating conservation of a core retinal metabolic program. Retinal metabolism is highly dependent on coordinated glycolytic and mitochondrial pathways to support photoreceptor function, neurotransmitter recycling, and cellular homeostasis (Aït-Ali *et al.*, 2015; Chinchore *et al.*, 2017; Hurley *et al.*, 2015). The altered abundance of glucose-associated metabolites, phosphorylated sugar intermediates, pyruvate-related metabolites, and TCA-cycle-associated metabolites observed in MRO is therefore consistent with differences in central carbon metabolism relative to native retina. Likewise, reduced abundance of glutamate-, aspartate-, and arginine-associated metabolites may reflect differences in neurotransmitter-associated metabolism and neuron–glia metabolic coupling, which are essential features of mature retinal tissue (Bringmann *et al.*, 2013). Differences were also observed in cholesterol, desmosterol, fatty acids, and phospholipid-associated metabolites. Lipid metabolism plays a critical role in membrane biosynthesis, photoreceptor outer segment formation, and synaptic organization (Fliesler and Bretillon, 2010). Pathway enrichment analysis further supported coordinated alterations in alanine–aspartate–glutamate metabolism, arginine biosynthesis, arginine and proline metabolism, glyoxylate and dicarboxylate metabolism, and starch and sucrose metabolism. Collectively, these pathways highlight selective differences in amino acid-associated and carbohydrate-associated metabolism between organoids and native retina (Xia and Zhang, 2022). The altered abundance of lipid- and sterol-associated metabolites may therefore be suggestive of incomplete photoreceptor-associated metabolic maturation under current culture conditions. Nevertheless, conservation of several fatty acid-associated metabolites indicates that major lipid metabolic pathways remain partially preserved during organoid differentiation (Fliesler and Bretillon, 2010).

Secretome dynamics during retinal organoid maturation

Analysis of conditioned media demonstrated dynamic extracellular metabolic remodeling during retinal organoid maturation. Temporal alterations were particularly evident in amino acid-associated and

carbohydrate-associated metabolites between early and late developmental stages. Previous studies have shown that developing retinal tissue and retinal organoids actively consume glutamate and aspartate during maturation (Li *et al.*, 2020), consistent with the patterns observed here. These findings support the concept of a retinal metabolic ecosystem in which metabolite exchange contributes to tissue development and homeostasis (Hanna *et al.*, 2025; Kanow *et al.*, 2017).

Implications for organoid optimization and future directions

The substantial overlap between MRO and native retina supports the utility of organoids as experimentally accessible models for investigating retinal development, inherited retinal degeneration, metabolic retinal disorders, and therapeutic interventions. At the same time, the metabolic differences identified in this study highlight potential targets for improving organoid maturation. Optimization of nutrient composition, oxygen availability, long-term culture conditions, retinal pigment epithelium interaction, and co-culture systems may improve metabolic fidelity and photoreceptor maturation. Future integration of metabolomics with transcriptomics, isotope-tracing approaches, and functional assays will further advance understanding of retinal organoid metabolic development. Recent studies increasingly emphasize that successful retinal organoid maturation requires not only appropriate cellular differentiation but also establishment of retina-specific metabolic programs and intercellular metabolic interactions (Fu *et al.*, 2021; Hanna *et al.*, 2025; Joyal *et al.*, 2018). The present findings contribute to this growing body of evidence by identifying both conserved retinal metabolic features and areas of selective metabolic divergence.

Limitations of the Study

The retinal organoid maturation may not be linearly equivalent to in vivo retinal development. Therefore, some metabolic differences observed between day 28 MRO and P1–P7 retina may reflect developmental asynchrony rather than incomplete differentiation alone. In addition, GCMS metabolomics measures relative metabolite abundance rather than metabolic flux or direct functional activity; therefore, we suggest to use such experiments to corroborate our findings. GCMS analysis also has limited sensitivity for complex lipids, retinoids, and low-abundance signaling molecules, potentially underrepresenting specific photoreceptor-associated metabolites. Therefore, targeted metabolomic analyses of specific metabolite classes would provide a more comprehensive understanding of these pathways. Furthermore, analysis was performed at a single developmental stage, whereas retinal metabolism is highly dynamic during maturation. Longitudinal metabolic profiling would therefore be valuable to distinguish delayed maturation from intrinsic organoid-associated limitations. Retinal organoids additionally lack several in vivo retinal features, including retinal pigment epithelium interaction and vascular-associated nutrient exchange, which may contribute to the metabolic differences observed between organoids and native retina.

5. Conclusion

In conclusion, MRO preserve a substantial conserved retinal metabolic signature while exhibiting selective metabolic divergence from native retina. Altered abundance of glycolysis-associated metabolites, TCA-cycle-associated metabolites, lipid-associated metabolites, and neurotransmitter-associated metabolites suggests incomplete metabolic maturation under current in vitro culture conditions. Nevertheless, the substantial overlap between MRO and native retina supports the utility of MRO as retina like metabolic systems. Identification of these metabolic differences provides a framework for future optimization strategies aimed at improving retinal organoid maturation and functional fidelity.

Declarations

Funding

This work was supported by DAAD (Deutscher Akademischer Austauschdienst) and Predoc Leipzig Award to PG and ZH, EFRE (Europäischer Fonds für regionale Entwicklung) grant CW and ERC (European Research Council NeuFRO - 101039764) to ZH, Hypatia fellow, Talent Track, Radboudumc to ZH.

Conflict of Interest

The authors declare no conflicts of interest.

Author Contribution Statement

ZH and PG conceived and designed the study. PG conducted experiments. retinal organoid culture, metabolomics experiments, data acquisition, and statistical analysis. ZH, CW contributed reagents and analytical tools. ZH and CW supervised the study, contributed to experimental design. PG and CW analyze the data and PG drafted the manuscript. ZH, CW, PK, FZ and JK contributed to data interpretation, and critical revision of the manuscript. All authors read and approved the final manuscript.

Compliance with Ethical Standards

All applicable international, national, and/or institutional guidelines for the care and use of animals were followed. All animal procedures were performed in accordance with institutional ethical regulations and approved protocols.

Data Availability Statement

The metabolomics and metadata reported in this paper are available in Radboud Data Repository https://doi.org/10.34973/ew8v-gp51.

Software or Database Availability Statement

Not applicable

Acknowledgments

The authors thank MS-UL core facility carried out analyses and Susan Billig, Ramona Oehme, Ferdinand Krause and Anastasia Orlova for technical assistance and support during metabolomics analysis.

References

1. Aït-Ali, N., Fridlich, R., Millet-Puel, G., Clérin, E., Delalande, F., Jaillard, C., Blond, F., Perrocheau, L., Reichman, S., Byrne, L. C., Olivier-Bandini, A., Bellalou, J., Moyse, E., Bouillaud, F., Nicol, X., Dalkara, D., van Dorsselaer, A., Sahel, J. A., & Léveillard, T. (2015). Rod-derived cone viability factor promotes cone survival by stimulating aerobic glycolysis. *Cell* 161, 817 – 32.
2. Bringmann, A., Grosche, A., Pannicke, T., & Reichenbach, A. (2013). GABA and Glutamate Uptake and Metabolism in Retinal Glial (Müller) Cells. *Front Endocrinol (Lausanne)*, *4*, 48.
3. Chen, H. Y., Kelley, R. A., & Swaroop, A. (2020). HIPRO: A High-Efficiency, Hypoxia-Induced Protocol for Generation of Photoreceptors in Retinal Organoids from Mouse Pluripotent Stem Cells. *STAR Protoc* 1.
4. Chinchore, Y., Begaj, T., Wu, D., Drokhlyansky, E., & Cepko, C. L. (2017). Glycolytic reliance promotes anabolism in photoreceptors. *Elife* 6.
5. Cowan, C. S., Renner, M., De Gennaro, M., Gross-Scherf, B., Goldblum, D., Hou, Y., Munz, M., Rodrigues, T. M., Krol, J., Szikra, T., Cuttat, R., Waldt, A., Papasaikas, P., Diggelmann, R., Patino-Alvarez, C. P., Galliker, P., Spirig, S. E., Pavlinic, D., Gerber-Hollbach, N., Schuierer, S., Srdanovic, A., Balogh, M., Panero, R., Kusnyerik, A., Szabo, A., Stadler, M. B., Orgül, S., Picelli, S., Hasler, P. W., Hierlemann, A., Scholl, H. P. N., Roma, G., Nigsch, F., & Roska, B. (2020). Cell Types of the Human Retina and Its Organoids at Single-Cell Resolution. *Cell*, *182*, 1623–1640e34.
6. Cui, Z., Guo, Y., Zhou, Y., Mao, S., Yan, X., Zeng, Y., Ding, C., Chan, H. F., Tang, S., Tang, L., & Chen, J. (2020). Transcriptomic Analysis of the Developmental Similarities and Differences Between the Native Retina and Retinal Organoids. *Invest Ophthalmol Vis Sci*, *61*, 6.
7. Du, J., Rountree, A., Cleghorn, W. M., Contreras, L., Lindsay, K. J., Sadilek, M., Gu, H., Djukovic, D., Raftery, D., Satrústegui, J., Kanow, M., Chan, L., Tsang, S. H., Sweet, I. R., & Hurley, J. B. (2016). Phototransduction Influences Metabolic Flux and Nucleotide Metabolism in Mouse Retina. *Journal Of Biological Chemistry*, *291*, 4698–4710.
8. Eiraku, M., Takata, N., Ishibashi, H., Kawada, M., Sakakura, E., Okuda, S., Sekiguchi, K., Adachi, T., & Sasai, Y. (2011). Self-organizing optic-cup morphogenesis in three-dimensional culture. *Nature*, *472*, 51–56.
9. Fliesler, S. J., & Bretillon, L. (2010). The ins and outs of cholesterol in the vertebrate retina. *Journal Of Lipid Research*, *51*, 3399–3413.
10. Fu, Z., Kern, T. S., Hellström, A., & Smith, L. E. H. (2021). Fatty acid oxidation and photoreceptor metabolic needs. *Journal Of Lipid Research*, *62*, 100035.

11. Hanna, J., David, L. A., Touahri, Y., Fleming, T., Screaton, R. A., & Schuurmans, C. (2022). Beyond Genetics: The Role of Metabolism in Photoreceptor Survival, Development and Repair. *Front Cell Dev Biol*, *10*, 887764.
12. Hanna, J., Touahri, Y., Pak, A., Belfiore, L., van Oosten, E., David, L. A., Han, S., Ilnytskyy, Y., Kovalchuk, I., Kurrasch, D., Okawa, S., Del Sol, A., Screaton, R. A., Aubert, I., & Schuurmans, C. (2025). Glycolytic flux controls retinal progenitor cell differentiation via regulating Wnt signaling. *Elife* 13.
13. Hurley, J. B., Lindsay, K. J., & Du, J. (2015). Glucose, lactate, and shuttling of metabolites in vertebrate retinas. *Journal Of Neuroscience Research*, *93*, 1079–1092.
14. Joyal, J. S., Gantner, M. L., & Smith, L. E. H. (2018). Retinal energy demands control vascular supply of the retina in development and disease: The role of neuronal lipid and glucose metabolism. *Progress In Retinal And Eye Research*, *64*, 131–156.
15. Kanow, M. A., Giarmarco, M. M., Jankowski, C. S., Tsantilas, K., Engel, A. L., Du, J., Linton, J. D., Farnsworth, C. C., Sloat, S. R., Rountree, A., Sweet, I. R., Lindsay, K. J., Parker, E. D., Brockerhoff, S. E., Sadilek, M., Chao, J. R., & Hurley, J. B. (2017). Biochemical adaptations of the retina and retinal pigment epithelium support a metabolic ecosystem in the vertebrate eye. *Elife* 6.
16. Kim, S., Lowe, A., Dharmat, R., Lee, S., Owen, L. A., Wang, J., Shakoor, A., Li, Y., Morgan, D. J., Hejazi, A. A., Cvekl, A., DeAngelis, M. M., Zhou, Z. J., Chen, R., & Liu, W. (2019). Generation, transcriptome profiling, and functional validation of cone-rich human retinal organoids. *Proc Natl Acad Sci U S A*, *116*, 10824–10833.
17. La Torre, A. (2016). Retinal differentiation of mouse embryonic stem cells. *Bio-protocol* 6, e1851-e1851.
18. Li, B., Zhang, T., Liu, W., Wang, Y., Xu, R., Zeng, S., Zhang, R., Zhu, S., Gillies, M. C., Zhu, L., & Du, J. (2020). Metabolic Features of Mouse and Human Retinas: Rods versus Cones, Macula versus Periphery, Retina versus RPE. *iScience* 23, 101672.
19. Li, C., Liu, W., Li, X., Lv, B., Qin, J., Yi, N., Xu, B., Xu, J., Xue, Z., Yan, H., & Xue, J. (2025). Metabolomic landscape of fetal organ development during late gestation in mice. *Commun Biol*, *8*, 1423.
20. Linsenmeier, R. A., & Dmitriev, A. V. (2024). Increased Retinal Metabolism Induced by Flicker in the Isolated Mouse Retina. *eNeuro* 11.
21. Ripps, H., & Shen, W. (2012). Review: taurine: a very essential amino acid. *Molecular Vision*, *18*, 2673–2686.
22. Sridhar, A., Hoshino, A., Finkbeiner, C. R., Chitsazan, A., Dai, L., Haugan, A. K., Eschenbacher, K. M., Jackson, D. L., Trapnell, C., Bermingham-McDonogh, O., Glass, I., & Reh, T. A. (2020). Single-Cell Transcriptomic Comparison of Human Fetal Retina, hPSC-Derived Retinal Organoids, and Long-Term Retinal Cultures. *Cell Rep*, *30*, 1644–1659e4.
23. Tsantilas, K. A., Cleghorn, W. M., Bisbach, C. M., Whitson, J. A., Hass, D. T., Robbings, B. M., Sadilek, M., Linton, J. D., Rountree, A. M., Valencia, A. P., Sweetwyne, M. T., Campbell, M. D., Zhang, H., Jankowski, C. S. R., Sweet, I. R., Marcinek, D. J., Rabinovitch, P. S., & Hurley, J. B. (2021). An Analysis

of Metabolic Changes in the Retina and Retinal Pigment Epithelium of Aging Mice. *Invest Ophthalmol Vis Sci*, *62*, 20.

24. Viegas, F. O., & Neuhauss, S. C. F. (2021). A Metabolic Landscape for Maintaining Retina Integrity and Function. *Frontiers In Molecular Neuroscience*, *14*, 656000.
25. Völkner, M., Kurth, T., Schor, J., Ebner, L. J. A., Bardtke, L., Kavak, C., Hackermüller, J., & Karl, M. O. (2021). Mouse Retinal Organoid Growth and Maintenance in Longer-Term Culture. *Front Cell Dev Biol*, *9*, 645704.
26. West, E. L., Majumder, P., Naeem, A., Fernando, M., O'Hara-Wright, M., Lanning, E., Kloc, M., Ribeiro, J., Ovando-Roche, P., Shum, I. O., Jumbu, N., Sampson, R., Hayes, M., Bainbridge, J. W. B., Georgiadis, A., Smith, A. J., Gonzalez-Cordero, A., & Ali, R. R. (2022). Antioxidant and lipid supplementation improve the development of photoreceptor outer segments in pluripotent stem cell-derived retinal organoids. *Stem Cell Reports*, *17*, 775–788.
27. Xia, M., & Zhang, F. (2022). Amino Acids Metabolism in Retinopathy: From Clinical and Basic Research Perspective. *Metabolites* 12.
28. Yera, M., Wang, J. J., & Zhang, S. X. (2025). Protocol for real-time assessment of energy metabolism in dissociated mouse retinal photoreceptors using a SeahorseXFe24 analyzer. *STAR Protoc*, *6*, 103595.
29. Zhao, J., Yao, K., Yu, H., Zhang, L., Xu, Y., Chen, L., Sun, Z., Zhu, Y., Zhang, C., Qian, Y., Ji, S., Pan, H., Zhang, M., Chen, J., Correia, C., Weiskittel, T., Lin, D. W., Zhao, Y., Chandrasekaran, S., Fu, X., Zhang, D., Fan, H. Y., Xie, W., Li, H., Hu, Z., & Zhang, J. (2021). Metabolic remodelling during early mouse embryo development. *Nat Metab*, *3*, 1372–1384.

Figures

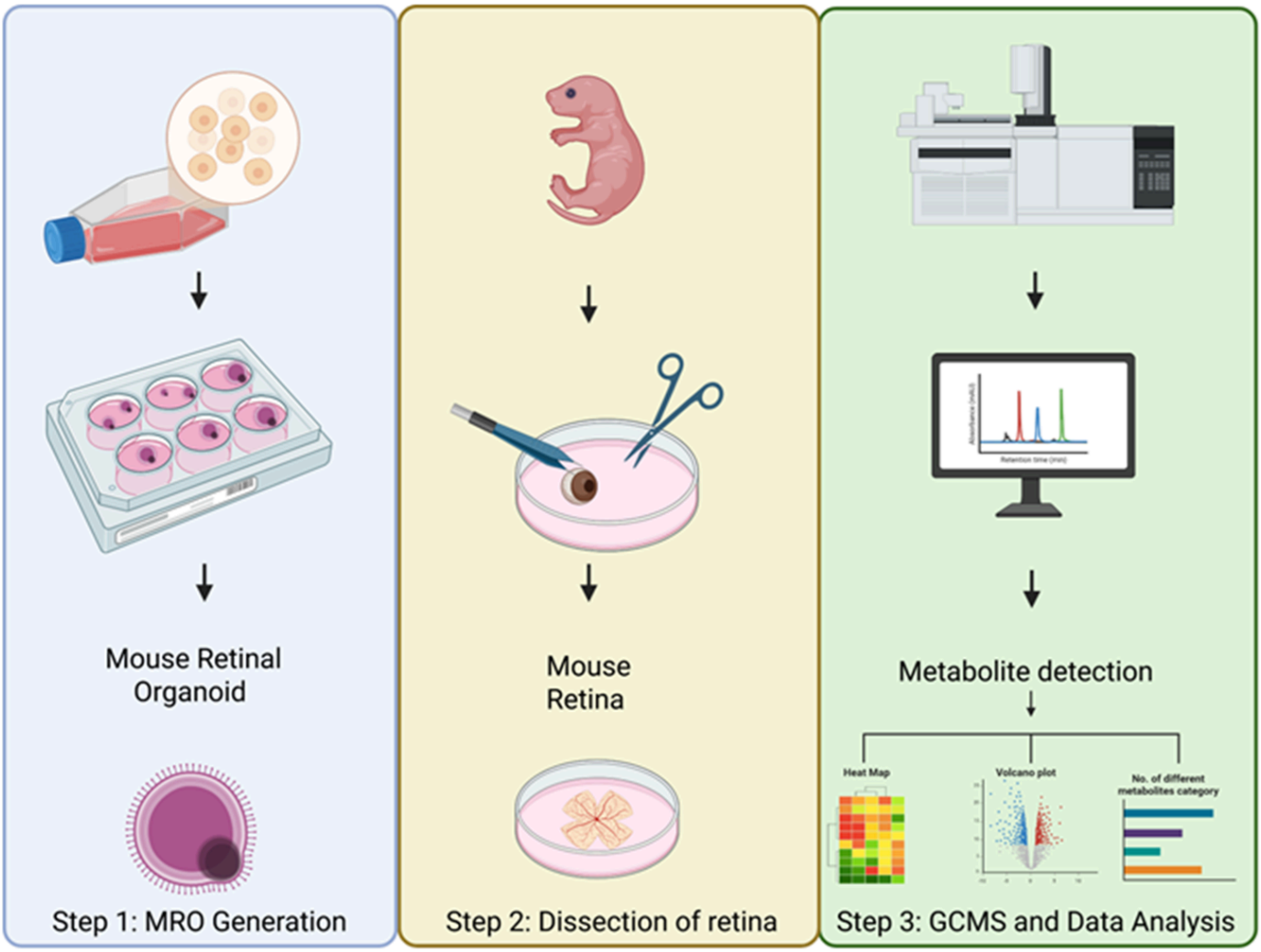


Figure 1

Schematic overview of the workflow for generating and metabolically profiling mouse MRO. Left panel (Step 1) shows the generation of MRO from ESD3 under controlled conditions to fully differentiated MRO. Middle panel (Step 2) shows isolation of native retina from neonatal wild type mice via eyeball excision and dissection. Right panel (Step 3) shows GCMS setup followed by metabolomic analysis. (Created in BioRender. Gupta, P. (2026) https://BioRender.com/gwz46yw)

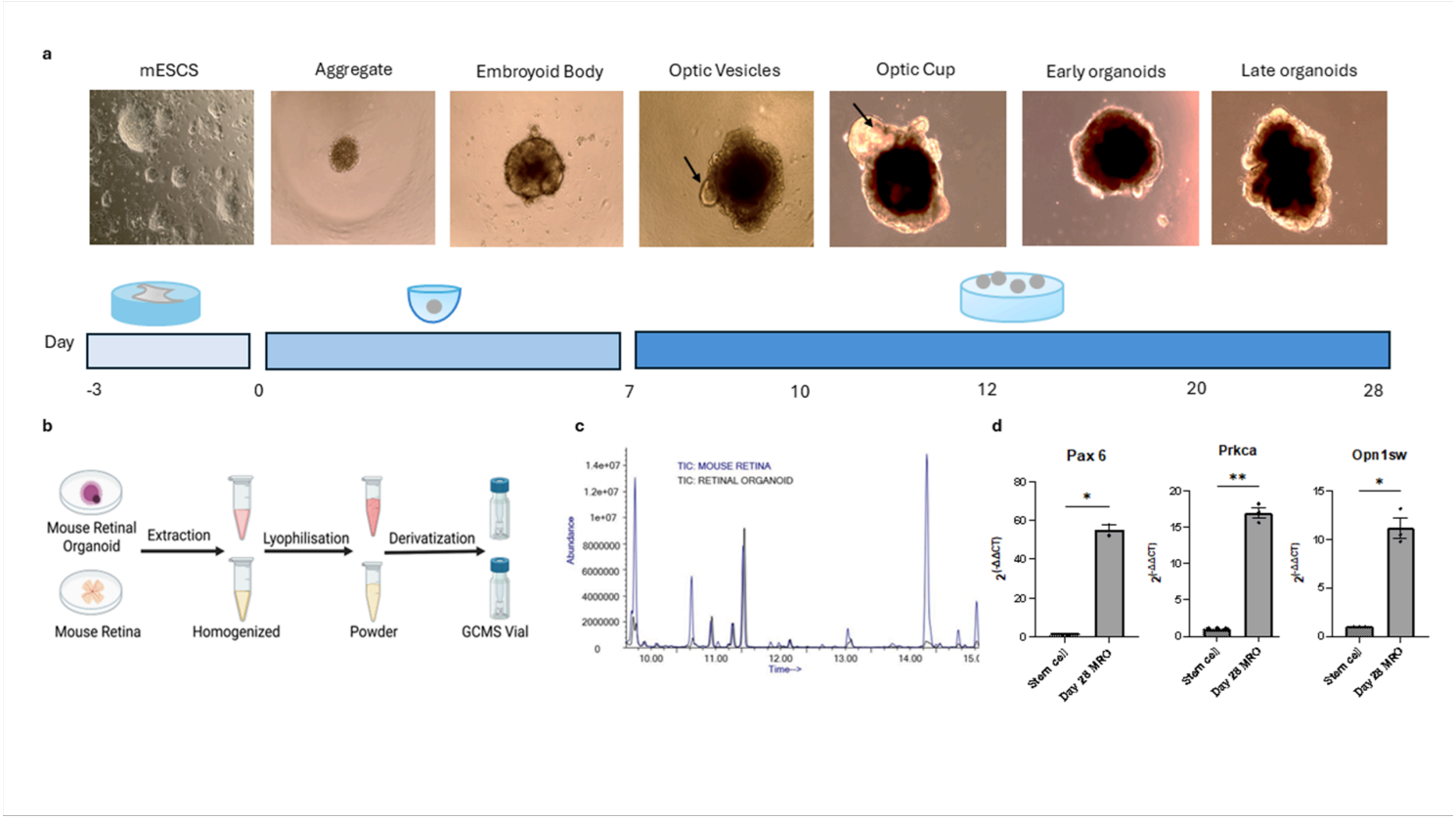


Figure 2

MRO generation, processing, total-ion chromatograms and cell type characterization. (a) Representative bright-field images illustrating key stages of retinal organoid differentiation from mouse embryonic stem cells (mESCs) to late organoids (day 28) were differentiated (Bio Protocols) Anna La Torre, 2016 and (b) Schematic of MRO and mouse retina tissue processing for metabolomic analysis (Created in BioRender. Gupta, P. (2026) https://BioRender.com/nc3z5cj) (c) Overlay of total-ion chromatograms (TICs) of mouse retina (blue trace) and MRO (black trace). (d) qPCR analysis showing relative expression of Pax6, Prkca, and Opn1sw in day-28 MROs. Data are presented as mean ± SEM from three independent retina/MRO batches. Statistical significance was determined using unpaired t-tests and is indicated as follows: ns, not significant ($P > 0.05$); *$P \leq 0.05$; **$P \leq 0.01$.

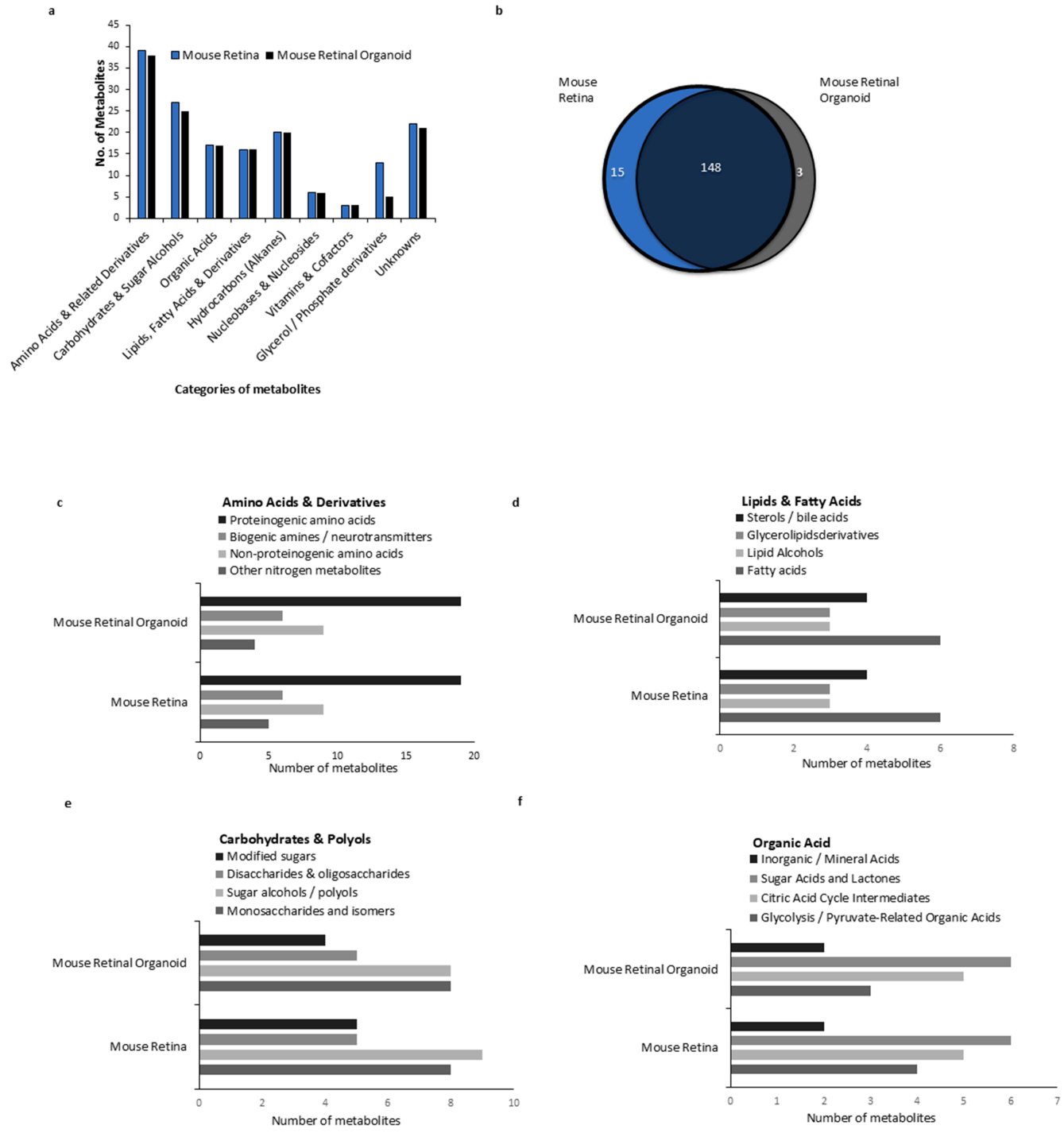


Figure 3

Comparative classification of detected metabolites in mouse retina and MRO. (a) Distribution of identified metabolites across major biochemical categories in mouse retina (blue) and retinal organoids (black). (b) Venn diagram showing shared and unique metabolites between mouse retina and MRO. (c–f) Subclassification of metabolites within amino acids and related derivatives, lipids and fatty acids,

carbohydrates and polyols, and organic acids in mouse retina and MRO. Bars represent the number of metabolites detected in each category.

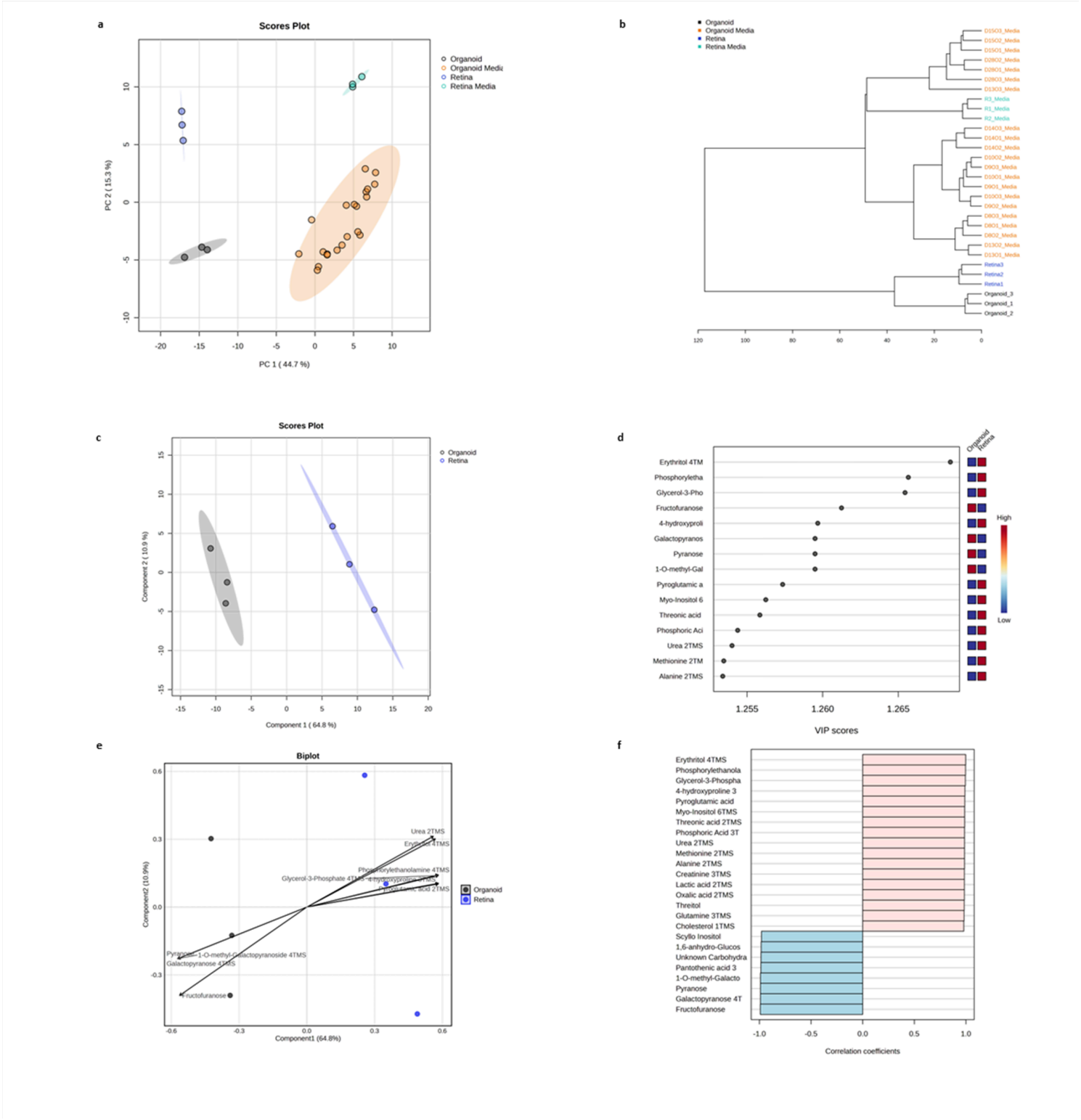


Figure 4

Clustering metabolites in mouse retina and MRO. (a) PCA score plot generated from normalized GCMS metabolite intensities of mouse retina, MRO, and their corresponding culture media (b) Hierarchical

clustering dendrogram constructed using distance-based clustering of metabolite profiles of mouse retina, MRO, and their culture media. (c) PLS-DA score plot showing separation between MRO and mouse retina. (d) VIP scores identifying metabolites that most strongly drive group separation between retinal organoids and retina. (e) Biplot showing metabolite distribution between MRO and native retina samples. Arrows represent metabolite loading vectors indicating metabolites contributing to sample separation. (f) Pattern correlation the top positive (pink) and negative (blue) correlated metabolites associated with the MRO–retina comparison.

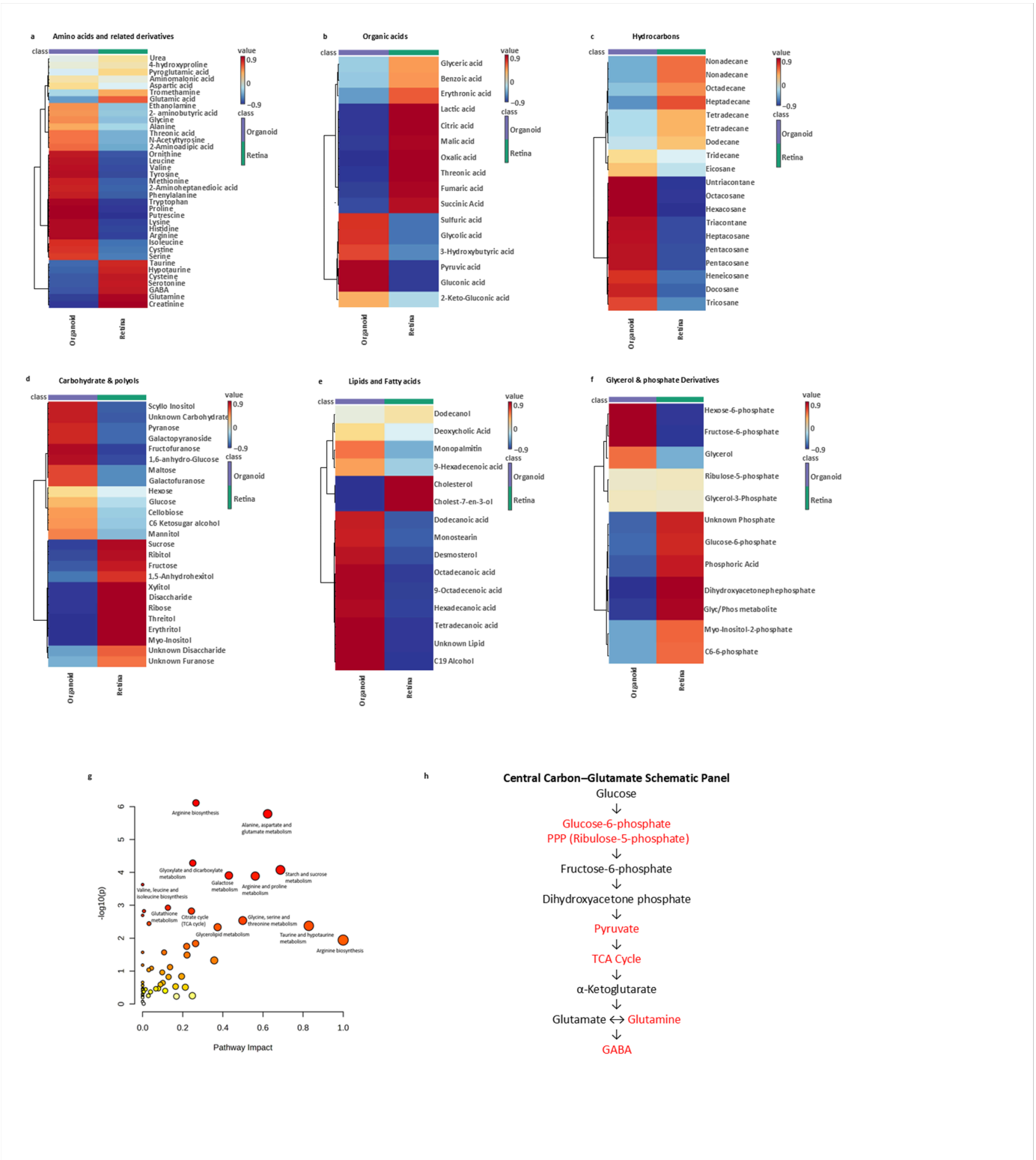


Figure 5

Hierarchical clustering heatmaps and pathway analysis of major metabolite subclasses. Clustered heatmaps of (a) Amino acids and related derivatives, (b) organic acid, (c) Hydrocarbons, (d) Carbohydrates and polyols, (e) lipids and fatty acids, and (f) Gycerol/phosphate derivatives. Rows represent metabolites and columns represent individual samples. Heatmaps display scaled relative abundances with unsupervised clustering applied to both metabolites and samples. (g) Pathway analysis showing altered metabolic pathways based on pathway impact and statistical significance (–log10 p-value). (h) Schematic proposed metabolic associated with carbon metabolism, contributing to neurotransmitter in MRO. Red indicated reduced metabolites.

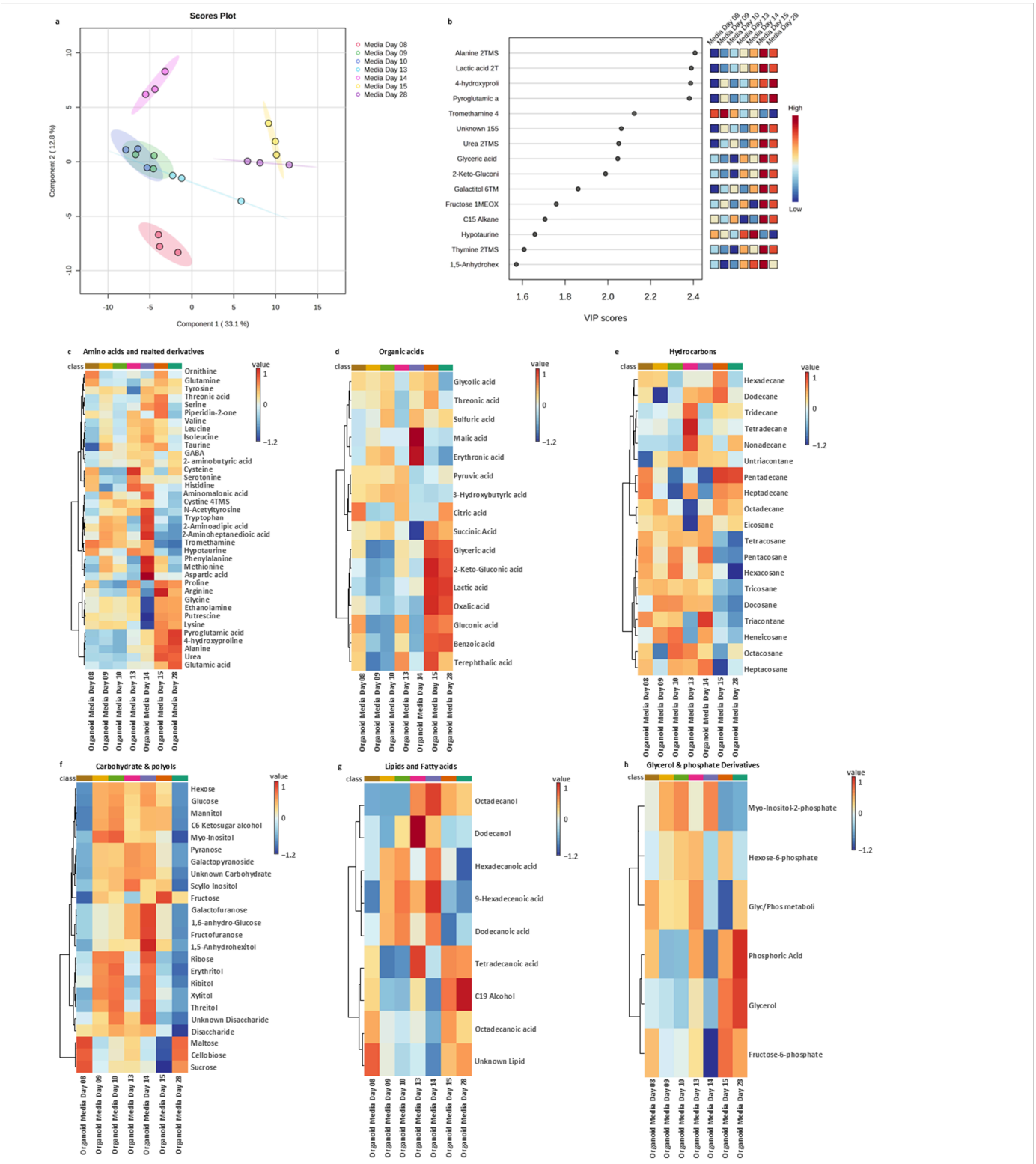


Figure 6

Multivariate discrimination and hierarchical clustering heatmaps of the MRO secretome at different developmental stages. (a) PLS-DA score plot showing separation MRO at different developmental stages. (b) Variable Importance in Projection (VIP) scores identifying metabolites that most strongly drive group separation between MRO and mouse retina. Hierarchical clustering heatmaps of major metabolite subclasses in MRO secretome at different days of collection.(c) Amino acids and related

derivatives, (d) organic acid, (e) Hydrocarbons, (f) Carbohydrates and polyols, (g) lipids and fatty acids, and (h) Gycerol/phosphate derivatives. Rows represent metabolites and columns represent individual samples.

Supplementary Files

This is a list of supplementary files associated with this preprint. Click to download.

- Supplementarytables.docx
- SupplementaryExcel2.csv
- SupplementaryExcel3.csv
- SupplementaryExcel4.csv
- SupplementaryExcel1.csv
- ChecklistSupplementary.pdf
- READMEFILE.docx
- SupplementryresultsandFigures.docx